Biosensors and Bioelectronics 45 (2013) 292–299

Contents lists available at SciVerse ScienceDirect

Biosensors and Bioelectronics

journal homepage: www.elsevier.com/locate/bios

Visible-light-activated photoelectrochemical biosensor for the study of acetylcholinesterase inhibition induced by endogenous neurotoxins

Qilin Huang [a,b], Hua Chen [a], Lili Xu [a], Danqin Lu [a], Linlin Tang [a], Litong Jin [a], Zhiai Xu [a,*], Wen Zhang [a,*]

[a] Department of Chemistry, East China Normal University, Shanghai 200062, P.R. China
[b] Department of Chemistry, Yuxi Normal University, Yuxi 653100, P.R. China

ARTICLE INFO

Article history:
Received 6 November 2012
Received in revised form
11 January 2013
Accepted 21 January 2013
Available online 14 February 2013

Keywords:
Photoelectrochemical biosensor
Acetylcholinesterase
Endogenous neurotoxin
Inhibition
Silver nanoparticles

ABSTRACT

In this report, a novel visible-light-activated photoelectrochemical biosensor was fabricated to study the inhibition of acetylcholinesterase (AChE) activity induced by two endogenous neurotoxins, 1(*R*)-methyl-6,7-dihydroxy-1,2,3,4-tetrahydroisoquinoline [(*R*)-Sal] and 1(*R*),2(*N*)-dimethyl-6,7-dihydroxy-1,2,3,4-tetra-hydroisoquinoline [(*R*)-NMSal], which have drawn much attention in the study of the pathogenesis of neurodegenerative diseases such as Parkinson's disease. The photoelectrode was prepared by three steps, as follows. At first, nitrogen and fluorine co-doped TiO_2 nanotubes (TNs) were obtained by anodic oxidation of a Ti sheet. Secondly, silver nanoparticles (AgNPs) were deposited onto the TNs through a microwave-assisted heating polyol (MAHP) process. At last, AChE was immobilized on the obtained photoelectrode and the biosensor was marked as AChE/Ag/N–F–TNs. Due to the nitrogen and fluorine co-doping, the photoelectrochemical biosensors can produce high photocurrent under visible light irradiation. Moreover, the presence of AgNPs greatly increased the photocurrent response of the biosensor. AChE/Ag/N–F–TNs hybrid system was used to study AChE inhibition induced by (*R*)-Sal and (*R*)-NMSal. The result proved that both (*R*)-Sal and (*R*)-NMSal exhibited mixed and reversible inhibition against AChE. This strategy is of great significance for the development of novel photoelectrochemical biosensors in the future.

1. Introduction

Photoelectrochemical biosensing, which employs potential (Hafeman et al., 1988) or current (Li et al., 2000) as a detection signal with light as an excitation source, is a burgeoning analytical technique presenting extremely high sensitivity due to the effective separation of excitation source from the detection signal (Tu et al., 2011). For photoelectrochemical detection, one of the most important aspects is to choose materials with high photoelectric conversion property, which include inorganic semiconductors, organic photoelectrical materials, composite materials and some kinds of biomacromolecules with photoelectrochemical activity. Typically, TiO_2, which is an important narrow band-gap semiconductor, has attracted much attention owing to its excellent photoelectric conversion efficiency, abundant resource and non-toxicity. However, as a result of the band gap (forbidden bandwidth) of TiO_2 being about 3.2 eV (anatase), only ultraviolet light ($\lambda < 387$ nm) can be absorbed by it (Anpo and Takeuchi, 2003). It not only means that the utilization of solar light is limited since UV light in solar light is less than 5%, but also biologic samples may be damaged by UV light in the process of the experiment (Li et al., 2011). Hence, to solve these problems and enhance the performance of the photoelectric sensor as well, much effort has been devoted to extend the excitation source of TiO_2 to the visible region by dye sensitization (Rominder et al., 1999), metal ion (May et al., 2009) and nonmetal atom doping (Asahi et al., 2001; Pan et al., 2011; Luo et al., 2004), semiconductor coupling (Sun et al., 2007), etc.

By doping TiO_2 with nonmetal atoms such as nitrogen (N) (Asahi et al., 2001; Pan et al., 2011), carbon (C) (Irie et al., 2003), and sulfur (S) (Ohno et al., 2004), the absorption edge of TiO_2 can be shifted to higher wavelength region. This is because nonmetal atoms can replace lattice oxygen with anionic dopant species and narrow the band gap of TiO_2. Particularly, N–F-codoped TiO_2 shows higher absorption than N-doped TiO_2 under visible light. At present, several research groups have reported the preparation of N–F-codoped TiO_2 by diverse methods such as the sol–gel-solvothermal method (Huang et al., 2006), spray pyrolysis (Li et al., 2005) and electrochemical anodization (Su et al., 2008). TiO_2 nanotubes (TNs) are of great interest due to their high surface-to-volume ratios and size-dependent properties. The

* Corresponding authors. Tel.: +86 021 62233509; fax: +86 021 62232627.
E-mail addresses: zaxu@chem.ecnu.edu.cn (Z. Xu), wzhang@chem.ecnu.edu.cn (W. Zhang).

0956-5663/$ - see front matter © 2013 Elsevier B.V. All rights reserved.
http://dx.doi.org/10.1016/j.bios.2013.01.075

N–F-codoped TiO_2 nanotubes (N–F–TNs) electrode presented an obvious synergetic effect and enhanced photocatalytic activity, and N–F–TNs have been successfully used in the research about photocatalytic degradation of organic compounds. In addition, noble metal modification is another important approach for improving the light absorption efficiency, catalytic and electronic efficiency of the composite system (Hirakawa and Kamat, 2005). Doping metal elements, such as gold (Au) (Li et al., 2007), platinum (Pt) (Formo et al., 2008), manganese (Mn) (Abuabara et al., 2007), silver (Ag) (Zhang et al., 2008), etc., has been reported in literature. Moreover, Ag is one of the most suitable candidates for industrial applications due to its low cost and ease of preparation (Lei and Ju, 2012). To the best of our knowledge, biosensors that use N–F–TNs with Ag deposit as substrate material have not yet been reported.

Parkinson's disease (PD) is a chronically progressive, age-related neurodegenerative disorder characterized by movement-related symptoms, cognitive and behavioral problems. Although the specific etiology of PD remains unclear, recently, the endogenous neurotoxins have been thought to play a major role in PD (Zhu et al., 2008). It was proved that 1(*R*)-methyl-6,7-dihydroxy-1,2,3,4-tetrahydroisoquinoline [(*R*)-Sal] concentrations in the urine and cerebrospinal fluid from patients of PD were significantly higher than those from controls, and 1(*R*),2(*N*)-dimethyl-6,7-dihydroxy-1,2,3,4-tetra-hydroisoquinoline [(*R*)-NMSal] was shown to induce a Parkinson syndrome in rats (Sandler et al., 1973; Moser and Kömpf, 1992; Naoi et al., 1996b). Endogenous neurotoxins might be related to the disruption of balance between dopamine and acetylcholine via the inhibition of acetylcholinesterase (AChE). In our previous work, it has been demonstrated that (*R*)-NMSal led to an inhibition effect on AChE activity, which could be closely associated with the development of PD. (Zhu et al., 2009).

In this work, we prepared a visible-light-activated photoelectrochemical biosensor for AChE to study AChE inhibition induced by [(*R*)-Sal] and [(*R*)-NMSal]. Firstly, N–F–TNs were prepared by anodic oxidation of the pure Titanium (Ti) sheet in the presence of $(NH_4)_2SO_4$ and NH_4F. Secondly, silver nanoparticles (AgNPs) were modified on the surface of N–F–TNs by the process of microwave–assisted heating polyol (MAHP). Lastly, AChE was immobilized onto the surface of Ag/N-F-TNs using chitosan as a crosslinker. After doping TNs with nitrogen, fluorine and silver, an obvious photocurrent signal could be observed when the prepared functional biosensor was exposed to visible light. Herein, we present a novel application of AChE-immobilized Ag/N–F–TNs (AChE/Ag/N–F–TNs) as a photoactive electrode for photoelectrochemical biosensing of acetylthiocholine (ATCh) under visible light irradiation. Moreover, the investigation of AChE inhibition induced by two endogenous neurotoxins was carried out. Analysis results reveal that the inhibition types of these two endogenous neurotoxins on AChE both belong to the reversible and mixed (competitive-uncompetitive) type.

2. Experimental

2.1. Chemicals and materials

AChE (type V-S, from electric eel), ATCh, (*R*)-Sal and (*R*)-NMSal were purchased from Sigma-Aldrich (St. Louis, MO, USA). $(NH_4)_2SO_4$, NH_4F, $AgNO_3$, KOH, ethylene glycol (EG) and chitosan (CS) were obtained from China National Medicines Corporation Ltd. (Beijing, China). Pieces of Ti sheet (dimensions: 15 mm × 5 mm × 0.5 mm, > 99% purity) were purchased from Tite Inc. (Shanghai, China). All other chemicals were of analytical grade. Phosphate buffer solution (PBS, 0.1 M) was prepared by using Na_2HPO_4 and KH_2PO_4. All solutions were prepared using Milli-Q (Millipore, Bedford, MA, USA) A-10 gradient (18 MΩ cm) deionized water.

2.2. Apparatus

Electrochemical experiments were done at room temperature with a CHI 832 electrochemical system (CH Instruments, Austin, TX, USA). Scanning electron microscopic (SEM) images were recorded by a Hitachi S4800 (Hitachi, Japan). The energy dispersive X-ray spectroscopy was measured and recorded by EDX Genesis fitted to the Hitachi FE-SEM S4800. For verification of the crystal structure of samples, for instance, Ti, N–F–TNs and Ag/N–F–TNs, the X-ray diffraction (XRD) analysis was done by a Rigaku Model D/max2550 (XRD, Model D/max 2550 V, Rigaku Co., Japan) using a diffractometer with monochromatized Cu KR radiation ($\lambda = 1.5418$ Å), performed over an angular range of $2\theta = 20°$–$90°$, scanned at a speed of 0.01°/s and steps of 0.01°. The equipment was operated at 35 KV and 25 mA. Reflectance spectra were measured and recorded in the range from 200 to 800 nm by a Hitachi, U-3900 (Hitachi, Japan) with an integrating sphere and with $BaSO_4$ as a reference. The surface chemical composition of the prepared samples was characterized by X-ray photoelectron spectroscopy (XPS, Kratos: Axis Ultra DLD) using Al-K_α monochromated radiation as the exciting source. The binding energy of the target elements (Ag, F, and N) was determined by using the banding energy of carbon (C 1s: 284.8 eV) as an internal standard.

2.3. Preparation of biosensors

2.3.1. Preparation of N–F–TNs

The Ti sheet was mechanically polished with abrasive papers of different fineness in sequence and rinsed in an ultrasonic bath of distilled water for 10 min. Subsequently, the Ti sheet was seriatim pretreated by sonicating in acetone, isopropyl alcohol and ethanol, then treated with the mixed solution of HF and HNO_3 ($HF:HNO_3:H_2O = 1:4:5$ in volume) for 1 min. After being treated as above, the Ti sheet was rinsed with acetone and deionized water for 10 min. Then the sheet was dried in air at room temperature. The highly ordered TiO_2 nanotube array electrodes were prepared by a similar electrochemical anodic oxidation technique reported by Macák's groups (Macák et al., 2005) and Lei's groups (Su et al., 2008). The anodization process was carried out at room temperature using a direct current power supply (HuGuang Electrical Appliance Co., Shanghai) in a cylindrical electrochemical reactor (the radius is 30 mm and height is about 70 mm), with the pretreated Ti sheet serving as the anode and carbon rod serving as the cathode. The electrolyte was 1 M $(NH_4)_2SO_4$ with the addition of small amounts of NH_4F (0.1 M). A potential of 20 V and anodization time of 120 min were used in this study. Anodized substrates were immediately rinsed with deionized water and dried with N_2 stream. Then, these substrates were annealed at 500 °C in air for 1 h to convert the amorphous phase to the anatase crystalline phase; both heating and cooling rates were kept at 2.5 °C/min.

2.3.2. Preparation of Ag/N–F–TNs substrate

The microwave–assisted heating polyol process was used to fabricate the Ag/N–F–TNs substrate according to that reported by Sifontes's group (Sifontes et al., 2010). The precursor solution was made by mixing 2.0 mL $AgNO_3$ (0.05 M) and 1.0 mL KOH (0.4 M) with 30 mL EG solution. The prepared N–F–TNs/Ti substrate was pretreated by sonicating in the mixture EG solution for several minutes and then treated by the microwave–assisted heating method for 50 s in the microwave oven (CW-2000, Shanghai Xintuo Analytical Instruments Co., Ltd., 500 W). After taking out, the prepared

Ag/N–F–TNs substrate was rinsed with acetone and deionized water three times, respectively, and then dried in air at room temperature.

2.3.3. Preparation of AChE/Ag/N–F–TNs biosensor

Afterwards, 10 μL enzyme solution containing 1.0 mg/mL of AChE, 1.2 mg/mL of BSA and 5.0 mg/mL chitosan was dropped on one side of the obtained Ag/N–F–TNs substrate and allowed to dry in air at room temperature. The obtained biosensor was denoted as AChE/Ag/N–F–TNs. For comparison, AChE/N–F–TNs biosensor was prepared by the same procedure except the process of loading AgNPs by the MAHP method. Both the modified biosensors were stored at 4 °C in a refrigerator before use. Before using the obtained biosensor, it was needed to rinse the electrode with deionized water to remove all physically absorbed materials.

2.4. Amperometric determination

A three-electrode system comprising the modified Ti sheet as working electrode, a platinum wire as auxiliary electrode and saturated calomel electrode (SCE) as reference electrode, was employed for all photoelectrochemical experiments. The electrolyte was the 0.1 M phosphate buffer (pH = 7.0). After being purged with highly purified nitrogen for at least 20 min, the electrochemical measurements were performed under a nitrogen atmosphere. A 500 W Xe lamp was used as the light source. The light source system was equipped with a 410 nm narrow-band filter. During the photoelectrochemical testing, the area of the working electrode was ca. 0.5 cm^2. After the background photocurrent was stabilized, the response was subsequently recorded as the excitation light was turned on and off.

3. Results and discussion

3.1. Design strategy of the photoelectrochemical biosensor

AChE, which is a member of the large class of serine esterases, plays an important role in the signal transduction process of the central nervous system. As a consequence, to study the activity change of AChE will contribute to the pathological study and the drug screening about injury and disease of the central nervous system. Therefore, a sensitive and stable AChE biosensor for the evaluation of AChE inhibition is urgently needed. AChE can exhibit catalytic activity towards substrate acetylcholine or ATCh (Zhu et al., 2008). Here, an AChE biosensor was fabricated for the detection of ATCh based on AgNPs-modified TNs. The procedure for the preparation of the AChE/Ag/N–F–TNs biosensor is described in Scheme 1. At first, nitrogen– and fluorine–doped TNs were obtained by electrochemical anodic oxidation of Ti sheets. Then, AgNPs were modified on the TNs by the MAHP method. So, the Ag/N–F–TNs nanocomposite for the photoelectrocatalytic oxidation of thiocholine, the product of ATCh hydrolyzation, was fabricated. Chitosan is frequently used as a suitable matrix for enzyme immobilization due to its low-cost and good biocompatibility (Luo et al., 2005). In this study, AChE was modified onto the surface of the electrode by chitosan.

As described in Scheme 1, in the presence of ATCh, AChE molecules immobilized on the Ag/N–F–TNs photoelectrode can hydrolyze ATCh into thiocholine and acetate. When the Ag/N–F–TNs photoelectrode was irradiated by the light source, electrons can be excited and move to the conduction band, leaving holes generated in the valence band. Then, thiocholine can act as a sacrificial electron donor for the holes generated upon excitation of the Ag/N–F–TNs (Zhu et al., 2009; Yissar et al., 2003). By monitoring the photocurrent, the concentration of ATCh can be

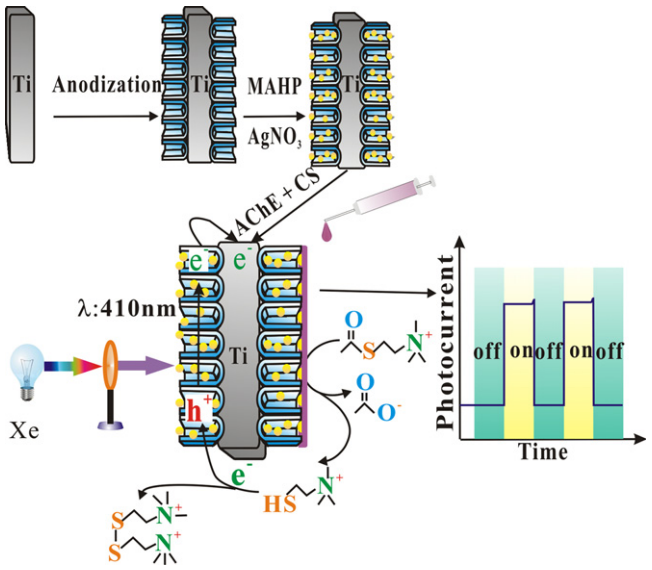

Scheme 1. Procedure for the preparation of the AChE/Ag/N–F–TNs biosensor and the schematic illustration for the photoelectrochemical detection of ATCh.

reflected. Therefore, the AChE/Ag/N–F–TNs photoelectrode can be used as a platform for the study of the inhibitory effect on AChE.

3.2. Characterization of as-prepared AChE/Ag/N–F–TNs

3.2.1. SEM and EDX characterization

During the preparation process, the surface morphologies and chemical composition of the biosensor's host materials changed. SEM and EDX were used as characterization techniques to record these modification processes and the morphology of prepared electrodes. Fig. 1(A) presents a top-view SEM image of the as-prepared porous TNs fabricated by anodic oxidation of a Ti sheet at 20 V for 2 h in 1 M $(NH_4)_2SO_4$ electrolyte containing 0.1 M NH_4F. As shown in the figure, an ordered porous structure of TNs is clearly observed, with an average pore diameter of ~30–50 nm and a wall thickness of ~15–30 nm. Thus, the average pore spacing was estimated to be approximately 90 nm. Therefore, the prepared TNs possess a self-organized structure with regular porous array. Fig. 1(E) presents the EDX spectrum of the as-prepared TNs. The strong diffraction peaks of elemental Ti at 0.45, 4.51 and 4.92 KeV are clearly seen. The diffraction peaks of elemental O, N and F are located at 0.52, 0.40 and 0.68 KeV, respectively. These results confirm that TNs were successfully doped with N and F by the one-step anodization method.

It has been proved that AgNPs can facilitate the improvement of the photoelectrochemical performance of semiconductor nanomaterials, as well as the immobilization of enzymes on nanotubes (May et al., 2009). Therefore, we deposited AgNPs on TNs in order to improve the performance of the biosensor. Fig. 1(B) is a high-magnification SEM image of the Ag/N–F–TNs electrode. We can see that the surface of the TNs electrode is covered with a large number of Ag NPs, which are spherical with uniform and narrow-dispersed size distribution. In addition, the inset SEM image also shows that AgNPs with diameter size of ~10–20 nm were distributed on N–F–TNs. Similarly, the EDX spectrum (Fig. 1(F)) confirms the presence of Ag and shows a content of about 1.18 at%. The above discussion demonstrates that it is an effective way to immobilize silver particles of nanosize on TNs by the MAHP process.

The low– and high– magnification SEM images of the prepared AChE/Ag/N–F–TNs are shown in Fig. 1(C and D). After the mixture composed of AChE and chitosan was immobilized on the surface of electrode, the microstructure of TNs could hardly be observed

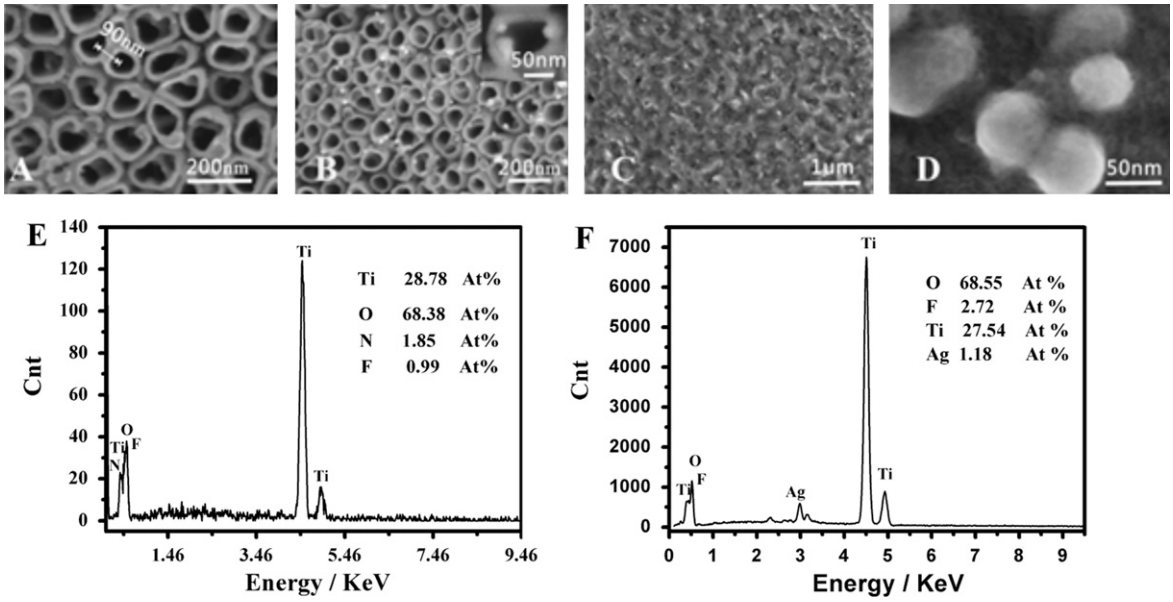

Fig. 1. SEM images of TNs (A), Ag/N–F–TNs (B), AChE/Ag/N–F–TNs with low (C) and high magnification (D); EDX spectra of N–F–TNs (E) and Ag/N–F–TNs (F).

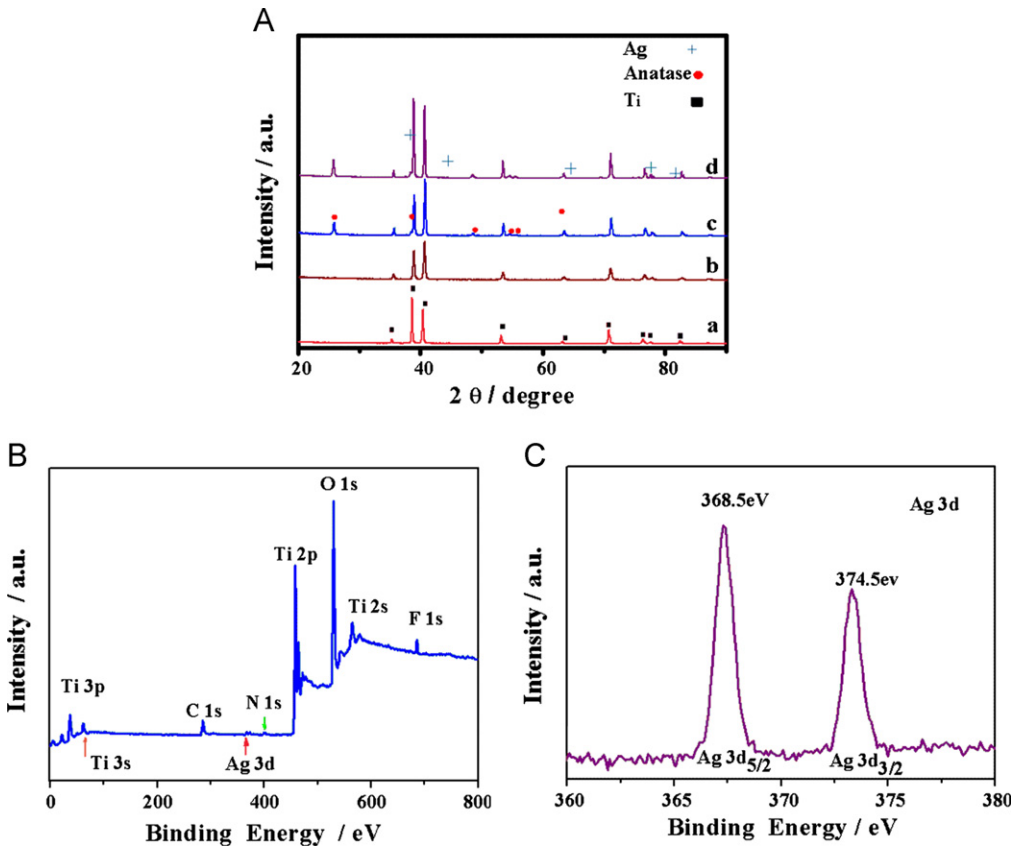

Fig. 2. (A) XRD patterns of Ti sheets (curve a), N–F–TNs before (curve b) and after (curve c) being annealed at 500 °C for 1 h, and Ag/N–F–TNs (curve d). XPS analysis results of the Ag/N–F–TNs sample (B) survey XPS spectrum and (C) high resolution spectrum for the Ag 3d states.

from the SEM images, and Ag NPs were covered by thin film, indicating that the film of AChE and chitosan was successfully immobilized on the surface of the electrode.

3.2.2. *XRD and XPS spectra of as-prepared electrodes*

To further establish the chemical properties of the Ag/N–F–TNs, XRD and XPS characterization were employed. Fig. 2(A) shows the XRD patterns of the prepared N–F–TNs electrode before and after being annealed at 500 °C for 1 h (curves b and c in Fig. 2(A)). For reference, the pattern of pure Ti sheet is also listed (curve a in Fig. 2(A)). As shown in the graph, the prepared TNs without annealing have almost the same diffraction peaks as that of Ti sheets, which indicates that the pristine TNs are amorphous or noncrystalline. However, after being annealed at 500 °C under air atmosphere for 1 h, the TNs sample has a

different XRD pattern with the appearance of diffraction peaks belonging to (101), (004), (200), (105), (211), and (204) planes of the anatase phase of TiO_2, which is favored for better photocatalytic oxidation reaction than the rutile phase (Pizem et al., 2002; Liu et al., 2009). Thus, these XRD results confirmed the successful preparation of phase-pure anatase TNs by the anodization process. In the curve d of Fig. 2(A), clear peaks of Ag (111), (200), (220), and (311), which are in good agreement with those reported in literature (Wang et al., 2009; Sano et al., 2003), further confirmed that AgNPs had been successfully deposited on TNs by the MAHP process.

Furthermore, the chemical states of the elements in the N–F–TNs and Ag/N–F–TNs were analyzed by XPS. Fig. 2(B) clearly indicates that five major sets of peaks from the N 1s, O 1s, Ti 2p, F 1s and Ag 3d states exist in the Ag/N–F–TNs sample. No trace of any impurity is observed, except for a small amount of adventitious carbon (C 1s) from the XPS instrument itself. Previous studies have shown that the $Ag3d_{5/2}$ binding energies for Ag, Ag_2O and AgO are approximately 368.2, 367.8 and 367.4 eV (Li et al., 2008; Wanger et al., 1979), respectively. And the $Ag3d_{3/2}$ binding energy for Ag is in the range 373.9–374.5 eV (Toledo-Antonio et al., 2009; Lai et al., 2010). The high-resolution XPS spectrum confined to the Ag3d window, as shown in Fig. 2(C), shows that the binding energies of Ag 3d doublet peaks located at 368.5 eV (Ag $3d_{5/2}$) and 374.5 eV (Ag $3d_{3/2}$), indicating that the doped Ag existed in a metallic form (Toledo-Antonio et al., 2009). These results are also in good agreement with the characterization of XRD, SEM, and EDX. Thus, these XRD and XPS results confirm the successful preparation of N–F–TNs by the anodization process and the deposition of Ag NPs by the MAHP process.

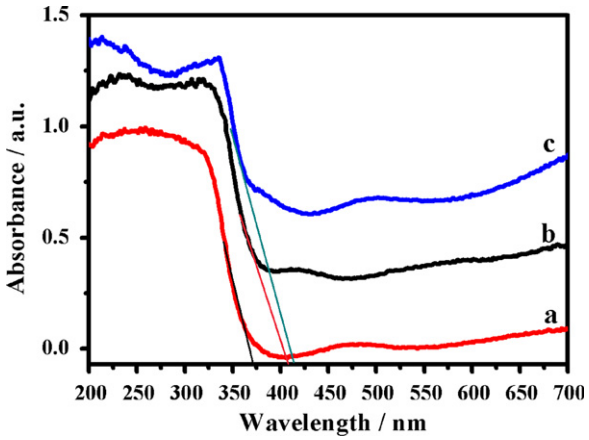

Fig. 3. UV–vis diffuse reflection spectra of (a) TNs (b) N–F–TNs and (c) Ag/N–F–TNs.

3.2.3. UV–vis diffuse reflection spectra of TNs, N–F–TNs, and Ag/N–F–TNs

To demonstrate the absorption edges of the fabricated electrodes, including TNs, N–F–TNs and Ag/N–F–TNs, the UV–vis diffuse reflection spectra are displayed in Fig. 3. The band gap of anatase TiO_2 is 3.2 eV (Anpo and Takeuchi, 2003) and TiO_2 has an absorption spectrum in the ultraviolet band ($\lambda < 387$ nm). Previous studies showed that N and F codoping could result in the increase of the absorption peak intensity in the visible region and the red-shift of stimulating wavelength (Pelaez et al., 2009). As shown in Fig. 3, compared with the undoped TNs sample which only has absorbance with wavelength below 387 nm (curve a), the N–F–TNs sample (curve b) shows obvious red-shift characteristics (absorption edge at about 407 nm). And the UV–vis spectrum shows that the prepared TNs upon doping have stronger absorption in the UV region and broader absorption in the visible region. The results are consistent with the previous reports (Asahi et al., 2001; Nakamura et al., 2004). Moreover, the absorption edge of Ag/N–F–TNs (curve c) is at about 414 nm which indicates that there is a slight red-shift compared with curve b. Furthermore, compared with curve b, there is a notable intensity change in curve c, which is because that Ag doping can increase the utilization rate of visible light (Paramasivam et al., 2007; Kyung et al., 2005). Ag/N–F–TNs sample presents a slightly broad absorption peak centered at 490 nm, which may originate from the surface plasmon resonance of Ag NPs (Lai et al., 2010). From the change of absorption edge, we can conclude that the band gap of the prepared Ag/N–F–TNs sample was decreased ($E_g < 3.0$ eV). It indicates that this hybrid nanomaterial could be excited under the visible light to promote the photocatalytic reaction.

3.3. Photoelectrochemical response of biosensor

At first, the influence of AgNPs size and amount on the photocurrent response was investigated. Along with the increase of MAHP time, the amount of AgNPs immobilized on the N–F–TNs increased, and larger AgNPs formed at the same time (Fig. S1A–D). When the MAHP time was 50 s, the photoelectrode gave the largest photocurrent response (Fig. S1E). Therefore, in the following modification process, 50 s was used as the MAHP process time. Fig. 4(A) gives a description of the time-based photocurrent responses of the AChE/N–F–TNs and AChE/Ag/N–F–TNs electrodes in the absence and presence of 0.1 mM ATCh upon light

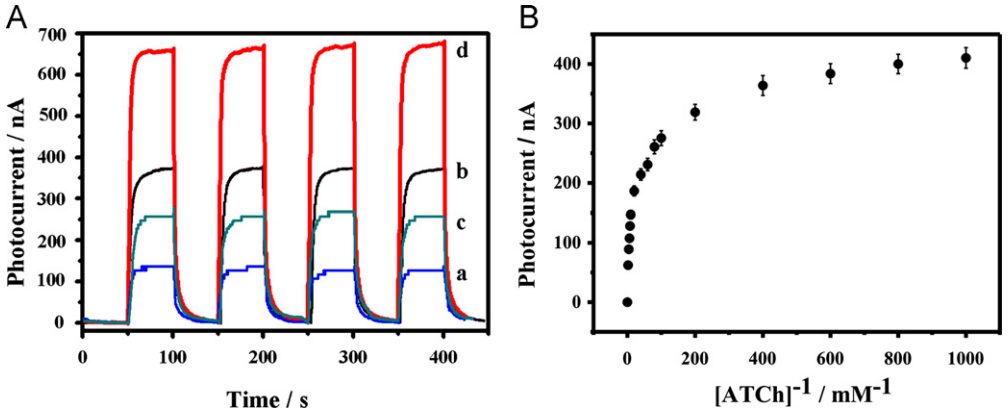

Fig. 4. (A) Photocurrent responses of (a) AChE/N–F–TNs and (b) AChE/Ag/N–F–TNs without ATCh and the responses of (c) AChE/N–F–TNs and (d) AChE/Ag/N–F–TNs in the presence of 0.1 mM ATCh. (B) Plot of the photocurrent vs. ATCh concentration for AChE/Ag/N–F–TNs biosensor. Data were recorded at a potential of 0.6 V in 0.1 M PBS (pH = 7.4) under nitrogen, and illumination with light of 410 nm. The illuminating light intensity was about 10 mW/cm^2.

irradiation in 0.1 M PBS solution. In the absence of ATCh, when the excitation light turned on, increased photocurrent of the AChE/N–F–TNs electrode was observable compared to that when the excitation light turned off (curve a). In the presence of ATCh, a marked enhancement of photocurrent compared to that in the absence of ATCh is clearly observed when the excitation light turned on (curve c). It can be explained by the mechanism described in Scheme 1. AChE can hydrolyze ATCh into thiocholine and acetate. When the N–F–TNs photoelectrode was irradiated by the light source, electrons in the valence band of TiO_2 could be promoted to the conduction band, generating electron/hole (e^-/h^+) pairs which could quickly move to the surface of N–F–TNs. Then, the thiocholine formed as the reaction proceeds could be oxidized easily and the photogenerated holes were captured directly by it, which promoted the separation between photoinduced charge and photoinduced hole, and then resulting in the increase of the photocurrent. The great increase of photocurrent in the presence of ATCh proves that the AChE molecules immobilized on the N–F–TNs photoelectrode keep the enzyme activity. Compared with the photocurrent responses of different electrodes without and with the deposition of AgNPs, it indicates that AChE/Ag/N–F–TNs electrode (curves b and d) had a higher photocurrent response than AChE/N–F–TNs electrode (curves a and c). In our work, we used the photocurrent increment ($\Delta I = I - I_0$, I and I_0 were the photocurrents of the electrode with or without ATCh) to evaluate AChE/N–F–TNs and AChE/Ag/N–F–TNs electrodes. It turns out that the photocurrent increment of the AChE/Ag/N–F–TNs electrode is about two times as that of the AChE/N–F–TNs electrode. These phenomena confirm the principal role of AgNPs in improving the performance of photoelectrochemical biosensor. The possible reason may be that AgNPs deposited on the TNs could improve the photoelectric conversion efficiency and photocatalytic activity (Kyung et al., 2005; Vamathevan et al., 2002).

The quantitative behavior of the photoelectrochemical biosensor was assessed by measuring the dependence of the increased photocurrent intensity on ATCh concentration. As shown in Fig. 4(B), at the AChE/Ag/N–F–TNs electrode, the generated photocurrent increases with the increase of the ATCh concentration (~1–400 μM) in solution. In this work, the detection limit of the AChE/Ag/N–F–TNs electrode to ATCh is 1 μM. This value is ten times lower than that reported in literature (Hai et al., 2006). This phenomenon was presumably ascribed to the excellent photoelectrocatalysis of AChE/Ag/N–F–TNs, suggesting a typical photoelectrocatalytic reduction process of ATCh. In this work, K_m values were calculated using the Lineweaver–Burk transformation of the Michaelis–Menten equation. The K_m value of the AChE linked to Ag/N–F–TNs towards ATCh is 5.861 μM. This value is lower than the previously reported value of 0.132 mM (Du et al., 2007). The lower K_m value for the AChE immobilized on Ag/N–F–TNs may be attributed to the photoelectrode host, which is a favorable kind of semiconductor nanomaterial providing good biocompatibility.

3.4. Reproducibility and stability of the photoelectrochemical biosensor

The reproducibility of the proposed photoelectrochemical biosensor was evaluated through the analysis of six independently prepared biosensors. The current response gave a relative standard deviation (R.S.D.) of 3.4% towards 0.1 mM ATCh, which

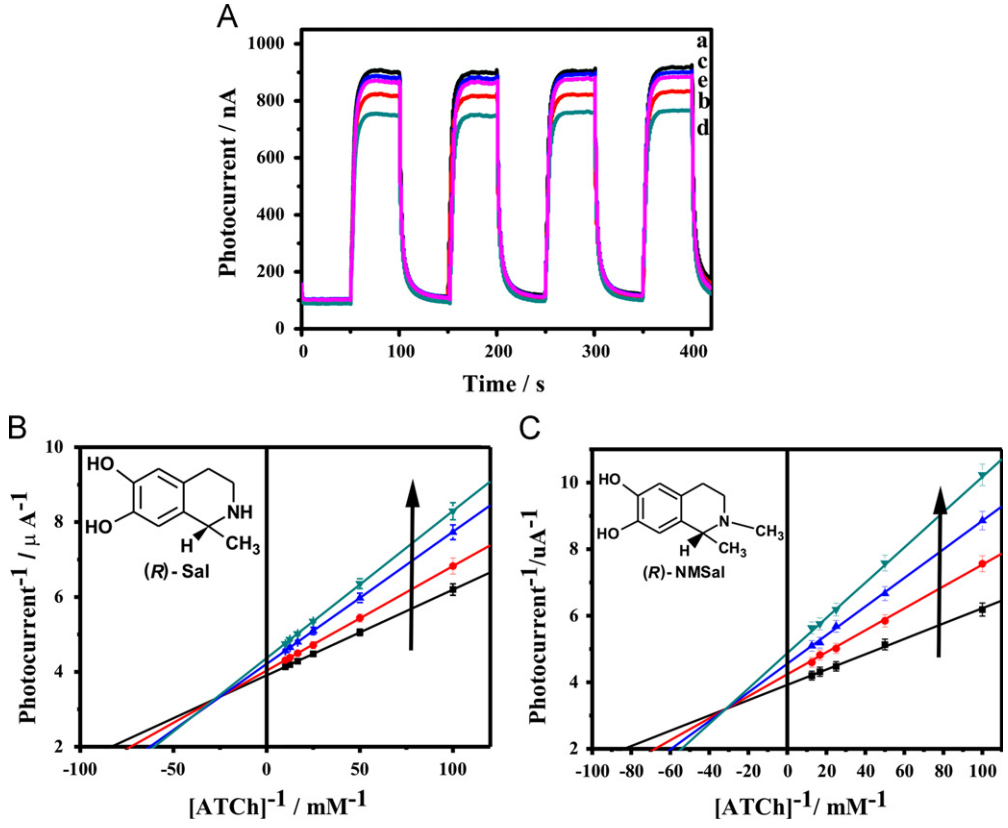

Fig. 5. (A) Photocurrent responses of the AChE/Ag/N–F–TNs photoelectrochemical system in the presence of 0.10 mM ATCh, (a) without the inhibitor, (b) with the addition of 0.1 μM (*R*)-Sal, (c) after exclusion of (*R*)-Sal, (d) with the addition of 0.1 μM (*R*)-NMSal, and (e) after exclusion of (*R*)-NMSal. (B) Lineweaver–Burke plots corresponded to the photocurrent of AChE/Ag/N–F–TNs at variable concentrations of ATCh in the presence of 0, 0.05 μM, 0.10 μM and 0.15 μM (*R*)-Sal. (C) The same as (B) but in the presence of 0, 0.05 μM, 0.10 μM and 0.15 μM (*R*)-NMSal. The arrowhead showed the increase of (*R*)-Sal or (*R*)-NMSal concentration. Data were recorded at a potential of 0.6 V in 0.1 M PBS (pH=7.4) under nitrogen, and illumination with light of 410 nm. The illuminating light intensity was about 10 mW/cm^2.

indicated an acceptable reproducibility and precision of the fabrication protocol described above. The stability of the AChE/Ag/N–F–TNs biosensor was tested by recording the photoelectrochemical current responses weekly for one month for electrodes stored in PBS solution at 4 °C. After 4 weeks of storage, the photocurrent responses still retained 90.1% value of the initial response, indicative of a quite satisfying stability.

3.5. Effect of (R)-Sal and (R)-NMSal on the photocurrent responses

Recently, in clinical research, it is found that AChE activity will be affected by various factors such as drug addicts, pesticides, heavy metal ions and neurotoxins, especially some endogenous neurotoxins. For instance, (*R*)-Sal and (*R*)-NMSal can disrupt the balance between dopamine (DA) and acetylcholine in striatum via the inhibition of AChE (Naoi et al., 1996a, 1996b; Maruyama et al., 1992). The prepared AChE/Ag/N-F-TNs hybrid photoelectrochemical system was used to examine the inhibition of (*R*)-Sal and (*R*)-NMSal on AChE. As shown in Fig. 5(A), there is a strong photocurrent response of AChE/Ag/N–F–TNs in the presence of 0.1 mM ATCh (curve a) upon the illumination and the decrease in the photocurrent can be observed with the addition of 0.1 μM (*R*)-Sal (curve b) and (*R*)-NMSal (curve d). Specifically, the photocurrent of curve b declines by 9.2% compared to curve a under the condition given above. But that of curve d declines by more than 14.9% with the same inhibitor concentration at the same determination condition. The results suggest that the inhibitory effect of (*R*)-Sal on AChE activity is less than that of (*R*)-NMSal. Because ATCh acts as a sacrificial electron donor to scavenge the holes (Yissar et al., 2003), the decrease of ATCh production weakens the accumulation of electrons in the conduction band of TNs, and then weakens the separation between the photogenerated electron and hole. When (*R*)-Sal or (*R*)-NMSal was added into the photoelectrochemical system, the increment of photocurrent would decrease gradually with the increase of their concentration. Another result of this study is that both (*R*)-Sal and (*R*)-NMSal lead to inhibition of AChE activity, but there is great difference in the extent of inhibition.

Fig. 5(B and C) shows the steady-state inhibition data graphically analyzed by Lineweaver–Burk plots. Double-reciprocal plots yield a group of lines intersecting at the second quadrant; the *y*-intercept corresponds to the reciprocal of maximal velocity (V_m), while the slope corresponds to the reciprocal of V_m/K_m. With the increase of endogenous neurotoxin concentration, Michaelis constants (K_m) increased and V_m decreased. These results indicate the occurrence of a reversible competitive-uncompetitive mixed type-I AChE inhibition (Su et al., 2008; Zhang et al., 2012). At the same time, we conclude that (*R*)-Sal and (*R*)-NMSal acting as inhibitor with their inhibitor constant (K_i) of 0.35 μM and 0.12 μM, respectively. The K_i values were obtained based on Dixon plot analysis (Fig. S2). By monitoring the inhibition ratio, linear ranges from 0.5 to 150 nM for (*R*)-Sal, and 1 to 200 nM for (*R*)-NMSal were obtained, respectively (Fig. S3). The corresponding detection limits were 0.1 nM and 0.2 nM for (*R*)-Sal and (*R*)-NMSal. These findings demonstrate that this photoelectrochemical system based on the prepared AChE/Ag/N–F–TNs biosensor could be applied to detect the ATCh and study the inhibition of AChE.

4. Conclusion

In summary, a novel and sensitive photoelectrochemical AChE biosensor based on Ag/N–F–TNs was fabricated for the determination of AChE inhibition induced by two endogenous neurotoxins, (*R*)-NMSal and (*R*)-Sal. The AChE/Ag/N–F–TNs biosensor showed an obvious photocurrent response under visible-light irradiation ($\lambda > 400$ nm), with significant photocurrent due to the specific one-dimensional array structure of N–F–TNs and AgNPs deposition onto the surface of TNs. Both (*R*)-Sal and (*R*)-NMSal exhibited a mixed inhibition against AChE. The inhibition constants K_i were obtained based on a Dixon plot analysis. The findings indicate that it can be used as a platform to investigate the relationship between the variations of the AChE activity and then study the AChE-related mechanism of PD.

Acknowledgment

This work was financially supported by the National Natural Science Foundation of China (No. 21075041) and Research Fund for the Doctoral Program of Higher Education of China (No. 2011007611003).

Appendix A. Supporting information

Supplementary data associated with this article can be found in the online version at http://dx.doi.org/10.1016/j.bios.2013.01.075.

References

Abuabara, S.G., Cady, C.W., Baxter, J.B., Schmuttenmaer, C.A., Grabtree, R.H., Brudvig, G.W., Batista, V.S., 2007. Journal of Physical Chemistry C 111, 11982–11990.
Anpo, M., Takeuchi, M., 2003. Journal of Catalysis 216, 505–516.
Asahi, R., Morikawa, T., Ohwaki, T., Aoki, K., Taga, Y., 2001. Science 293, 269–271.
Formo, E., Lee, E., Campbell, D., Xia, Y.N., 2008. Nano Letters 8, 269–672.
Hafeman, D.G., Parcej, W., Mcconnell, H.M., 1988. Science 240, 1182–1185.
Hai, A., Ben-Haim, D., Korbakov, N., Cohen, A., Shappir, J., Oren, R., Spira, M.E., Yitzchaik, S., 2006. Biosensors and Bioelectronics 22, 605–612.
Hirakawa, T., Kamat, P.V., 2005. Journal of the American Chemical Society 127, 3928–3934.
Huang, D.G., Liao, S.J., Liu, J.M., Dang, Z., Petrik, L., 2006. Journal of Photochemistry and Photobiology A 184, 282–288.
Irie, H., Watanabe, Y., Hashimoto, K., 2003. Chemistry Letters 32, 772–773.
Kyung, H., Lee, J., Choi, W., 2005. Environmental Science and Technology 39, 2376–2382.
Lai, Y.K., Zhuang, H.F., Xie, K.P., Gong, D.G., Tang, Y.X., Sun, L., Lin, C.J., Chen, Z., 2010. New Journal of Chemistry 34, 1335–1340.
Lei, J.P., Ju, H.X., 2012. Chemical Society Reviews 41, 211–2134.
Li, D., Haneda, H., Hishita, S., Ohashi, N., 2005. Chemistry of Materials 17, 2588–2595.
Li, H.B., Li, J., Xu, Q., Hu, X.Y., 2011. Analytical Chemistry 83, 9681–9686.
Li, H.X., Bian, Z.F., Zhu, J., Huo, Y.N., Li, H., Lu, Y.F., 2007. Journal of the American Chemical Society 129, 4538–4539.
Li, Q.W., Luo, G.A., Feng, J., Cai, D.W., Ouyang, Q., 2000. Analyst 125, 1908–1910.
Li, Y.Z., Zhang, H., Guo, Z.M., Han, J.J., Zhao, X.J., Zhao, Q.N., Kim, S.J., 2008. Langmuir 24, 8351–8357.
Liu, S.J., Wu, X.X., Hu, B., Gong, J.Y., Yu, S.H., 2009. Crystal Growth and Design 9, 1511–1518.
Luo, H.M., Takata, T., Lee, Y., Zhao, J.F., Domen, K., Yan, Y.S., 2004. Chemistry of Materials 16, 846–849.
Luo, X.L., Xu, J.J., Wang, J.L., Chen, H.Y., 2005. Chemical Communications 16, 2169–2171.
Macák, J.M., Tsuchiya, H., Schmuki, P., 2005. Angewandte Chemie International Edition 44, 2100–2102.
Maruyama, W., Nakahara, D., Ota, M., Takahashi, T., Takahashi, A., Nagatsu, T., Naoi, M., 1992. Journal of Neurochemistry 59, 395–400.
May, R.A., Patel, M.N., Johnston, K.P., Stevenson, K.J., 2009. Langmuir 25, 4498–4509.
Moser, A., Kömpf, D., 1992. Life Science 50, 1885–1891.
Du, D., Huang, X., Cai, J., Zhang, A., Ding, J., Chen, S., 2007. Analytical and Bioanalytical Chemistry 387, 1059–1065.
Nakamura, R., Tanaka, T., Nakato, Y., 2004. Journal of Physical Chemistry B 108, 10617–10620.
Naoi, M., Maruyama, W., Dostert, P., Kohda, K., Kaiya, T., 1996a. Neuroscience Letters 212, 183–186.
Naoi, M., Maruyama, W., Dostert, P., Hashizume, Y., Nakahara, D., Takahashi, T., Ota, M., 1996b. Brain Research 709, 285–295.
Ohno, T., Akiyoshi, M., Umebayashi, T., Asai, K., Mitsui, T., Matsumura, M., 2004. Applied Catalysis A: General 265, 115–121.
Pan, J.H., Han, G., Zhou, R., Zhao, X.S., 2011. Chemical Communications 47, 6942–6944.

Paramasivam, I., Macak, J.M., Ghicov, A., Schmuki, P., 2007. Chemical Physics Letters 445, 233–237.
Pelaez, M., Cruz, A.A., Stathatos, E., Falaras, P., Dionysiou, D.D., 2009. Catalysis Today 144, 19–25.
Pizem, H., Sukenik, C.N., Sampathkumaran, U., McIlwain, A.K., Guire, M.R.D., 2002. Chemistry of Materials 14, 2476–2485.
Rominder, P.S., Liu, J.B., Crittenden, J.C., Hand, D.W., 1999. Journal of the Air and Waste Management Association 49, 951–958.
Sandler, M., Bonham, S., Hunter, K.R., Stern, G.M., 1973. Nature (London) 241, 439–443.
Sano, T., Negishi, N., Uchino, K., Tanaka, J., Matsuzawa, S., Takeuchi, K., 2003. Journal of Photochemistry and Photobiology A 160, 93–98.
Sifontes, Á.B., Melo, L., Maza, C., Mendes, J.J., Mediavilla, M., Brito, J.L., Zoltan, T., Albornoz, A., 2010. Química Nova 33, 1266–1269.
Su, Y.L., Zhang, X.W., Zhou, M.H., Han, S., Lei, L.C., 2008. Journal of Photochemistry and Photobiology A 194, 152–160.
Sun, W.T., Yu, Y., Pan, H.Y., Gao, X.F., Chen, Q., Peng, L.M., 2007. Journal of the American Chemical Society 130, 1124–1125.
Toledo-Antonio, J.A., Cortes-Jácome, M.A., Angeles-Chavez, C., López-salinas, E., Quintana, P., 2009. Langmuir 17, 10195–10201.
Tu, W.W., Lei, J.P., Wang, P., Ju, H.X., 2011. Chemistry: A European Journal 17, 9440–9447.
Vamathevan, V., Amal, R., Beydoun, D., Low, G., McEvoy, S., 2002. Journal of Photochemistry and Photobiology A 148, 233–245.
Wanger, C.D., Riggs, W.M., Davis, L.E., Moulder, J.F., Muilenberg, G.E., 1979. Handbook of X-ray photoelectron spectroscopy. Perkin-Elmer Corporation, Physical Electronics Division, Eden Prairie, Minnesota, USA 90.
Wang, P.T., Guo, J.B., Wang, H.H., Zhang, Y., Wei, J., 2009. Journal of Physical Chemistry C 133, 8118–8123.
Yissar, V.P., Katz, E., Wasserman, J., Willner, I., 2003. Journal of the American Chemical Society 125, 622–623.
Zhang, H., Wang, G., Chen, D., Lv, X.J., Li, J.H., 2008. Chemistry of Materials 20, 6543–6549.
Zhu, W., An, Y.R., Luo, X.M., Wang, F., Zheng, J.H., Tang, L.L., Wang, Q.J., Zhang, Z.H., Zhang, W., Jin, L.T., 2009. Chemical Communications 19, 2682–2684.
Zhu, W., Wang, D., Zheng, J.H., An, Y.R., Wang, Q.J., Zhang, W., Jin, L.T., Gao, H.Y., Lin, L.N., 2008. Clinical Chemistry 54, 705–712.
Zhang, Y.D., Hei, T.T., Cai, Y.N., Gao, Q.Q., Zhang, Q., 2012. Analytical Chemistry 84, 2830–2836.